Polyp-DAM: Polyp segmentation via depth anything model

Zhuoran Zheng[1], Chen Wu[2], Wei Wang[3], Yeying Jin[4], and Xiuyi Jia[1]

[1] Nanjing University of Science and Technology
[2] University of Science and Technology of China
[3] Sun Yat-sen University
[4] National University of Singapore
zhengzr@njust.edu.cn

Abstract. Recently, large models (Segment Anything model) came on the scene to provide a new baseline for polyp segmentation tasks. This demonstrates that large models with a sufficient image level prior can achieve promising performance on a given task. In this paper, we unfold a new perspective on polyp segmentation modeling by leveraging the Depth Anything Model (DAM) to provide depth prior to polyp segmentation models. Specifically, the input polyp image is first passed through a frozen DAM to generate a depth map. The depth map and the input polyp images are then concatenated and fed into a convolutional neural network with multiscale to generate segmented images. Extensive experimental results demonstrate the effectiveness of our method, and in addition, we observe that our method still performs well on images of polyps with noise. The URL of our code is https://github.com/zzr-idam/Polyp-DAM.

Keywords: Large models · Polyp segmentation · Depth anything model · Depth map · Convolutional neural network.

1 Introduction

The appearance of polyps in the intestine is a precursor to rectal cancer [17]. Therefore, the detection of polyps is of great importance for the early diagnosis and treatment of rectal cancer. However, manual screening by physicians usually leads to the problem of underdetection and misdetection. So far, automated polyp segmentation methods provide physicians with accurate decision-making.

Currently, several automated polyp segmentation methods based on deep learning have been developed and made significant progress [32,20,5,23,34,2,11,33]. In particular, the large model-based approach [2,11,33] (SAM) provides a new baseline for polyp segmentation. The outstanding performance of these methods on the polyp problem benefits from the role of large models that carry a large number of prior image levels. However, SAM-based methods require large computational resources to fine-tune polyp segmentation datasets, and the fine-tuning results are fraught with uncertainty. To address this problem, we use
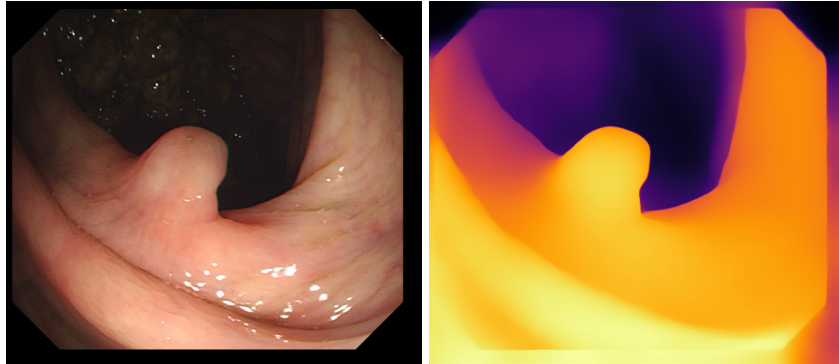
Fig. 1. This figure shows the result of processing a polyp image using DAM, which distinguishes the polyp (foreground) from the rest of the image (background) very well.
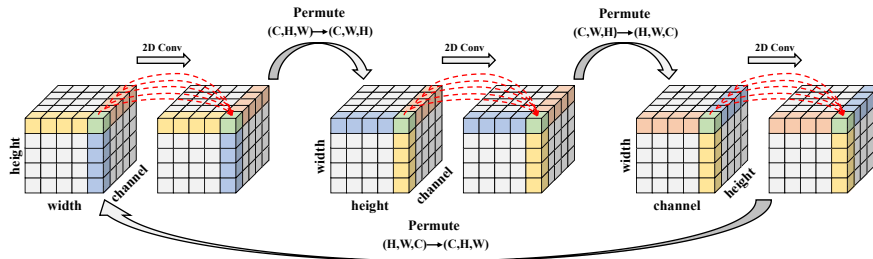
Fig. 2. This figure shows the process of processing our global module. Here, the transformation of the feature map dimension is followed by filtering using a 1×1 convolution, similar to performing an attention operation on this dimension.

the image-level prior (see Figure 1) provided by the Depth Anything Model (DAM) [28,9] to explicitly construct a polyp segmentation model, which does not require fine-tuning of the larger model.

In this paper, we propose a simple but effective polyp segmentation method, named Polyp-DAM. Specifically, first, the input polyp image is performed by the DAM to obtain a depth image corresponding to the polyp. Depth images and polyp images are sampled to four different sizes and fed into our designed multi-scale MixNet (M^2ixNet). M^2ixNet is inspired by the vanilla MLP-Mixer [21], but different from it, the global module encodes the feature maps of images from the perspectives of the width W, height H, and channel C (see Figure 2). Through dimensional transformation operations (`permute`), the information encoded in each feature map is associated and fused. Note that dimension transformation operations do not introduce additional parameters, which means that by permuting the feature maps from different views, the global module achieves efficient modeling of long-range dependency. Furthermore, to efficiently model the local features of the feature map, we design a local feature capture module. The local module filters the feature maps produced by the global module through a 3D

convolution for local modeling (here the feature map is viewed as a grid). Finally, the four feature maps output by M^2ixNet with different scales are fused by a 2D convolution to obtain a mask corresponding to a polyp image.

- To the best of our knowledge, we are the first to introduce the DAM prior to the polyp image segmentation task. The DAM can assist the segmentation model in distinguishing between foreground and background.
- We propose M^2ixNet, which efficiently performs the segmentation of polyp images through global versus local modeling. It is worth noting that the number of parameters in our network is only **0.47M** without considering DAM.
- Extensive experiments demonstrate that our method outperforms state-of-the-art approaches with better quantitative and qualitative evaluation.

2   Related Work

UNet [16] is a classical image segmentation model with a symmetric encoding-decoding architecture, and it can efficiently fuse shallow and deep features of an image. Based on its good segmentation performance, some polyp segmentation methods [29,14,27,15] adopt the U-shape network. In addition, some methods use attention mechanisms and carefully designed strategies to improve segmentation accuracy [8,25,31,34,24,30,3,19]. Recently, since the success of the Transformer in multiple fields, some approaches [4,23,5,2,11,33] have replaced the backbone of networks from CNN with Transformer and obtained good results. In this paper, we focus on obtaining accurate polyp image segmentation results using an image-level prior.

3   Method

An overview of Polyp-DAM is shown in Fig. 3. For a given polyp image $\mathbf{X} \in \mathbb{R}^{H \times W \times 3}$, we start by projecting $\mathbf{X}$ onto a 4-level resolution image $\{\mathbf{X}_o, \mathbf{X}_{64}, \mathbf{X}_{128}, \mathbf{X}_{256}\}$ by using the bilinear interpolation. Then, we input $\mathbf{X}$ into the DAM to generate a depth map $\mathbf{D} \in \mathbb{R}^{H \times W \times 3}$, which is also projected onto the image at 4 levels of resolution $\{\mathbf{D}_o, \mathbf{D}_{64}, \mathbf{D}_{128}, \mathbf{D}_{256}\}$. Finally, these depth maps of different resolutions with corresponding polyp images are input into the M^2ixNet to get an accurate mask $\mathbf{M}$. Here, different scales of polyp information are input into a convolutional layer (3×3 convolution kernel) in pairs respectively, followed by output feature maps up-sampled to the resolution of the original image. It is worth noting that the accurate mask $\mathbf{M}$ was also mapped to 4 resolutions to do loss in the training stage for the GT $\mathbf{O}$.

3.1   Global Module of M^2ixNet

The polyp images at different scales and the corresponding depth images are convolved to obtain a feature map $\mathbf{F}_0 \in \mathbb{R}^{H \times W \times 12}$ by concatenating them on
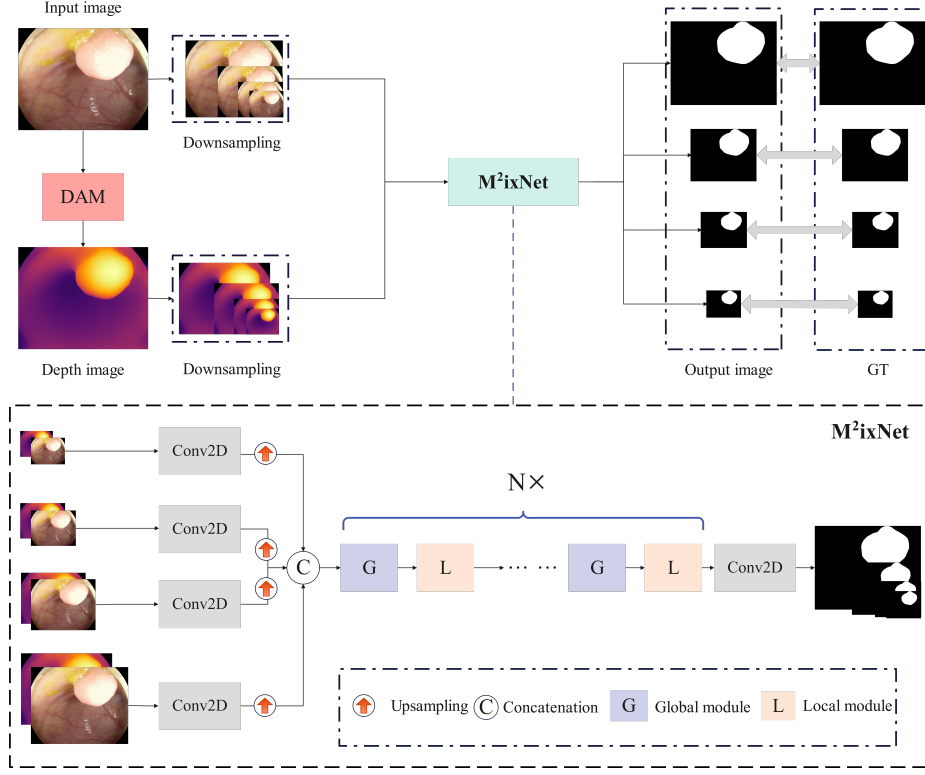
Fig. 3. The structure of our method. First, we obtain the depth map of the input polyp image via DAM. Next, the input image and depth map are bilinearly downsampled into 256×256, 128×128, 64×64, and the original resolution is fed into M^2ixNet. Finally, our network outputs four masks of different sizes and four sizes generated on GT for learning. It is worth noting that our network used in the evaluation on the benchmark is the image at the model output original resolution.

the channel domain, respectively. After that, $\mathbf{F}_0$ is fed into the global module G initially. G is designed from [21]. We try to capture the long-range dependence of polyp images using a small number of operators. Specifically, we first adjust the normalized input features' resolution, then perform some dimension transformation operations on them. Given the input feature $\mathbf{F}_0$, this procedure can be written as:

$$\mathbf{F}_1 = \mathrm{IP}(\mathbf{F}_0), \tag{1}$$

$$\hat{\mathbf{F}}_1 = \underbrace{\mathrm{Permute}(\mathrm{ReLU}(\mathrm{Conv}_{1\times 1}(\mathbf{F}_1)))}_{\times 3}, \tag{2}$$

where $\hat{\mathbf{F}}_t$ is intermediate result. $\mathrm{IP}(\cdot)$ corresponds to the interpolation operation, $\mathrm{Conv}_{1\times 1}(\cdot)$ is a 1×1 convolution, $\mathrm{ReLU}(\cdot)$ represents ReLU function, $\mathrm{Permute}(\cdot)$

denotes the dimension transformation operation and $\times 3$ denotes three operations in sequence. It is worth noting that before executing the last dimension transformation operation, we replace the ReLU function with the Sigmoid function.

Afterward, We use interpolation to adjust the feature $\hat{\mathbf{F}}_t$ to its original resolution to estimate the attention map and adaptively modulate the input $\mathbf{F}_0$ according to the estimated attention via element-wise product. This process can be written as:

$$\mathbf{F}_g = \text{IP}(\hat{\mathbf{F}}_1) \odot \mathbf{F}_0, \tag{3}$$

where $\mathbf{F}_g$ are the final output features and $\odot$ represents element-wise product.

3.2 Local Module of $\mathbf{M}^2\mathbf{ixNet}$

For local feature extraction, we mainly use a 3D convolution to perform on the input feature map. Specifically, given the inputs $\mathbf{F}_0$ and $\mathbf{F}_g$, they are expanded by one dimension thus obtaining $\hat{\mathbf{F}}_0 \in \mathbb{R}^{1 \times H \times W \times C}$ and $\hat{\mathbf{F}}_g \in \mathbb{R}^{1 \times H \times W \times C}$. Next, $\hat{\mathbf{F}}_0$ and $\hat{\mathbf{F}}_g$ are concatenated in the newly expanded dimensions to obtain a tensor $\mathbf{B} \in \mathbb{R}^{2 \times H \times W \times C}$. Then, we use a 3D convolution to extract the features of $\mathbf{B}$ to yield a new feature map $\mathbf{F}_2 \in \mathbb{R}^{H \times W \times C}$(here the input channel of the 3D convolution is 2 and the output channel is 1). Finally, $\mathbf{F}_2$ passes through a convolutional block (including two convolutional layers with 3×3 convolutional kernels) to obtain a feature map that is summed with $\mathbf{F}_0$ performing the corresponding element. The above process can be written:

$$\mathbf{F}_l = \text{ConvB}(\text{Conv3D}(\text{Cat}(\text{UnSqu}(\mathbf{F}_0), \text{UnSqu}(\mathbf{F}_g)))) + \mathbf{F}_0, \tag{4}$$

where $\mathbf{F}_l$ are the final output features, UnSqu denotes the expanded dimension, ConvB denotes the convolution block and $+$ represents the element-wise sum.

In this paper, we use 32 pairs of global and local modules. Among other things, we use a lot of shortcuts between modules. At the output of the network, a 2D convolution is used to squeeze the channels of the feature map to 1.

3.3 Loss Function

Our loss function can be formulated as :

$$\mathcal{L} = \mathcal{L}_{IoU}^w + \mathcal{L}_{BCE}^w, \tag{5}$$

where $\mathcal{L}_{IoU}^w$ and $\mathcal{L}_{BCE}^w$ represent the weighted intersection over union loss and weighted binary cross entropy loss [26], which are adopted for the global and local restriction. Deep supervision is performed on the four stage outputs (*i.e.*, $\mathbf{M}_o$, $\mathbf{M}_{64}$, $\mathbf{M}_{128}$ and $\mathbf{M}_{256}$). Each output is up-sampled to the same size as the ground truth $\mathbf{O} \in \{\mathbf{O}_o, \mathbf{O}_{64}, \mathbf{O}_{128}, \mathbf{O}_{256}\}$. The total loss can be formulated as:

$$\mathcal{L}_{total} = \sum_{i=1}^{i=4} \mathcal{L}(\mathbf{M}_i, \mathbf{O}_i) \tag{6}$$

In this paper, we use the output of $\mathbf{M}_o$ as the segmented image generated by the model. Note that, except for the original image resolution $\mathbf{M}_o, \mathbf{O}_o$, all other images are obtained by bilinear interpolation.
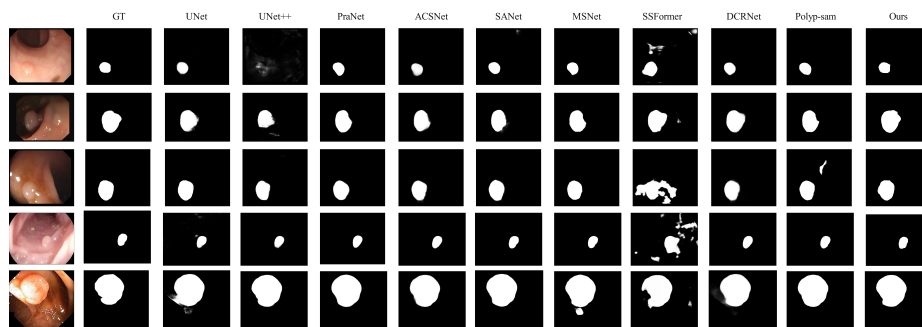
Fig. 4. Our method exhibits the best visual results.

4   Experiment

4.1   Implementation Details

We implement our model in the PyTorch 2.0 framework. The GPU shader is NVIDIA TITAN RTX 3090 with 24G RAM. During training, all input images are uniformly resized to 352×352 and a multi-scale training strategy [8] is employed. The network is trained for 200 epochs with a batch size of 16. For optimizer, we use the AdamW [12] to update parameters. The learning rate is 1e-4 and the weight decay is 1e-4.

4.2   Datasets and Metrics

To evaluate the performance of the proposed M^2ixNet, we follow the popular experimental setups [8], which adopt 5 publicly available benchmarks: Kvasir-SEG [10], CVC-ClinicDB [1], ColonDB [20], Endoscene [22] and ETIS [18]. The training set comprises 900 images from Kvasir-SEG and 550 from CVC-ClinicDB. The remaining 100 images from Kvasir-SEG and 62 images from CVC-ClinicDB are used as test sets. Since they are already seen during training, we use them to assess the learning ability of our model. We perform testing using ColonDB, Endoscene, and ETIS, as these datasets are not used during the training stage, they are utilized to measure the generalization ability of our model.

Following previous work [8,4], We employ six widely-used metrics for quantitative evaluation, including Mean Dice Similarity Coefficient (mDice), mean Intersection over Union (mIoU), Mean Absolute Error (MAE), weighted F-measure (F_β^w) [13], S-measure (S_α) [6], and max E-measure (E_ξ^{max}) [7]. mDice and mIoU are similarity measures at the regional level, while MAE and F_β^w are utilized to evaluate the pixel-level accuracy. S_α and E_ξ^{max} are used to analyze global-level similarity. The lower value is better for the MAE and the higher is better for others.

Table 1. Quantitative results on Kvasir-SEG [10] and CVC-ClinicDB [1] dataset. **Bold** indicates the best performance.

method	Year	mDice	mIoU	F_β^w	S_α	E_ξ^{max}	MAE
Kvasir-SEG							
UNet [16]	2015	0.818	0.746	0.794	0.858	0.893	0.055
UNet++ [35]	2018	0.821	0.744	0.808	0.862	0.909	0.048
PraNet [8]	2020	0.898	0.841	0.885	0.915	0.948	0.030
ACSNet [31]	2020	0.898	0.838	0.882	0.920	0.952	0.032
SANet [25]	2021	0.904	0.847	0.892	0.915	0.953	0.028
MSNet [32]	2021	0.902	0.847	0.891	0.923	0.954	0.029
SSFormer [23]	2022	**0.925**	0.878	0.921	0.931	0.969	**0.017**
DCRNet [29]	2022	0.846	0.772	0.807	0.882	0.917	0.053
Polyp-sam [11]	2023	0.900	0.860	-	-	-	-
M^{2}ixNet(Ours)	2024	**0.929**	**0.881**	**0.929**	**0.935**	**0.971**	**0.014**
CVC-ClinicDB							
UNet [16]	2015	0.823	0.755	0.811	0.890	0.953	0.019
UNet++ [35]	2018	0.794	0.729	0.785	0.873	0.931	0.022
PraNet [8]	2020	0.899	0.849	0.896	0.937	0.979	0.009
ACSNet [31]	2020	0.882	0.826	0.873	0.928	0.959	0.011
SANet [25]	2021	0.916	0.859	0.909	0.940	0.976	0.012
MSNet [32]	2021	0.915	0.867	0.912	0.947	0.978	0.008
SSFormer [23]	2022	0.916	0.873	0.924	0.947	0.971	0.007
DCRNet [29]	2022	0.869	0.800	0.832	0.919	0.968	0.023
Polyp-sam [11]	2023	0.920	0.870	-	-	-	-
M^{2}ixNet (Ours)	2024	**0.941**	**0.891**	**0.934**	**0.955**	**0.989**	**0.005**

4.3   Experiments with State-of-the-art Methods

We compare the proposed D^{2}LNet with previous state-of-the-art methods, including Polyp-sam [11], DCRNet [29], SSFormer [23], MSNet [32], SANet [25], ACSNet [31], PraNet [8], UNet++ [35], UNet [16]. For a fair comparison, we use their open-source codes to evaluate the same datasets or use the predictions provided by themselves.

Quantitative Comparison. As can be seen in Table 1 and Table 2, M^{2}ixNet achieves the best scores across five datasets on almost all metrics.

Visual Comparison. Figure 4 shows the visualization results of our model and the compared models. Our proposed model significantly outperforms other methods with better segmentation results, which are the closest to the ground truth. We discover that our model possesses the following advantages: Our model can adapt to different lighting conditions, such as the overexposure observed in the third and sixth images in Figure 4. This is thanks to the role of the image-level prior that DAM brings into play.

4.4   Ablation Study

We conduct an ablation study to validate the effectiveness of the modules designed in our M^{2}ixNet. To validate the effectiveness of the DAM, we removed the role of depth map (w/o DAM). To analyze the effectiveness of the multi-scale input information, We use only the original polyp images as input (w/o

Table 2. Quantitative results on ColonDB [20], Endoscene [22] and ETIS [18]) dataset. **Bold** indicates the best performance.

method	Year	mDice	mIoU	F_β^w	S_α	E_ξ^{max}	MAE
		CVC-ColonDB					
UNet [16]	2015	0.504	0.436	0.491	0.710	0.781	0.059
UNet++ [35]	2018	0.481	0.408	0.467	0.693	0.763	0.061
PraNet [8]	2020	0.712	0.640	0.699	0.820	0.872	0.043
ACSNet [31]	2020	0.716	0.649	0.697	0.830	0.851	0.039
SANet [25]	2021	0.752	0.669	0.725	0.837	0.875	0.043
MSNet [32]	2021	0.747	0.668	0.733	0.837	0.883	0.042
SSFormer [23]	2022	0.772	0.697	0.766	0.844	0.883	0.036
DCRNet [29]	2022	0.661	0.576	0.613	0.767	0.828	0.110
Polyp-sam [11]	2023	**0.894**	0.843	-	-	-	-
$\mathbf{M^2ixNet}$ **(Ours)**	2024	0.820	**0.855**	**0.799**	**0.869**	**0.935**	**0.021**
		Endoscene					
UNet [16]	2015	0.710	0.627	0.684	0.843	0.875	0.022
UNet++ [35]	2018	0.707	0.624	0.687	0.839	0.898	0.018
PraNet [8]	2020	0.871	0.797	0.843	0.925	0.968	0.010
ACSNet [31]	2020	0.863	0.787	0.825	0.923	0.968	0.013
SANet [25]	2021	0.888	0.815	0.859	0.928	0.972	0.008
MSNet [32]	2021	0.862	0.796	0.846	0.927	0.953	0.010
SSFormer [23]	2022	0.887	0.821	0.869	0.929	0.962	0.007
DCRNet [29]	2022	0.753	0.670	0.689	0.854	0.900	0.025
Polyp-sam [11]	2023	**0.905**	**0.860**	-	-	-	-
$\mathbf{M^2ixNet}$ **(Ours)**	2024	0.895	**0.861**	**0.879**	**0.941**	**0.978**	**0.005**
		ETIS					
UNet [16]	2015	0.398	0.335	0.366	0.684	0.740	0.036
UNet++ [35]	2018	0.401	0.343	0.390	0.683	0.776	0.035
PraNet [8]	2020	0.628	0.567	0.600	0.794	0.841	0.031
ACSNet [31]	2020	0.578	0.509	0.530	0.754	0.764	0.059
SANet [25]	2021	0.750	0.654	0.685	0.849	0.897	0.015
MSNet [32]	2021	0.720	0.650	0.675	0.846	0.881	0.020
SSFormer [23]	2022	0.767	0.698	0.736	0.863	0.891	0.016
DCRNet [29]	2022	0.509	0.432	0.437	0.714	0.787	0.053
Polyp-sam [11]	2023	**0.905**	0.861	-	-	-	-
$\mathbf{M^2ixNet}$ **(Ours)**	2024	0.891	**0.866**	**0.753**	**0.882**	**0.933**	**0.009**

Table 3. Ablation study for M^2ixNet on the Kvasir-SEG [10] dataset.

	mDice	mIoU	F_β^w	S_α	E_ξ^{max}	MAE
w/o DAM	0.874	0.840	0.882	0.899	0.930	0.049
w/o multi-scale	0.911	0.876	0.920	0.910	0.969	0.020
$\mathbf{M^2ixNet}$	**0.929**	**0.881**	**0.929**	**0.935**	**0.971**	**0.014**

multi-scale). Table 3 demonstrates the performance of the model without the DAM and multi-scale drops sharply on Kvasir datasets.

5   Discussion and Conclusion

We try to feed the depth maps generated by DAM as supplementary information to the UNet and UNet++ models, and on the Kvasir-SEG [10] dataset, their

performance improves by **5**% and **8**%, respectively. Especially on extremely exposed datasets, DAM is also capable of generating high-quality depth maps to assist polyp segmentation models.

In this paper, we use the DAM-assisted polyp segmentation model to achieve accurate polyp segmentation. Furthermore, our proposed M^2ixNet shows efficient segmentation. Experimental results demonstrate the superiority of our method.

References

1. Bernal, J., Sánchez, F.J., Fernández-Esparrach, G., Gil, D., Rodríguez, C., Vilariño, F.: WM-DOVA maps for accurate polyp highlighting in colonoscopy: Validation vs. saliency maps from physicians. CMIG **43**, 99–111 (2015) 6, 7
2. Biswas, R.: Polyp-sam++: Can a text guided sam perform better for polyp segmentation? arXiv preprint arXiv:2308.06623 (2023) 1, 3
3. Chi, L., Jiang, B., Mu, Y.: Fast fourier convolution. Advances in Neural Information Processing Systems **33**, 4479–4488 (2020) 3
4. Dong, B., Wang, W., Fan, D.P., Li, J., Fu, H., Shao, L.: Polyp-pvt: Polyp segmentation with pyramid vision transformers. arXiv preprint arXiv:2108.06932 (2021) 3, 6
5. Duc, N.T., Oanh, N.T., Thuy, N.T., Triet, T.M., Dinh, V.S.: Colonformer: An efficient transformer based method for colon polyp segmentation. IEEE Access **10**, 80575–80586 (2022) 1, 3
6. Fan, D.P., Cheng, M.M., Liu, Y., Li, T., Borji, A.: Structure-measure: A new way to evaluate foreground maps. In: Proceedings of the IEEE international conference on computer vision. pp. 4548–4557 (2017) 6
7. Fan, D.P., Gong, C., Cao, Y., Ren, B., Cheng, M.M., Borji, A.: Enhanced-alignment measure for binary foreground map evaluation. arXiv preprint arXiv:1805.10421 (2018) 6
8. Fan, D.P., Ji, G.P., Zhou, T., Chen, G., Fu, H., Shen, J., Shao, L.: Pranet: Parallel reverse attention network for polyp segmentation. In: International conference on medical image computing and computer-assisted intervention. pp. 263–273. Springer (2020) 3, 6, 7, 8
9. Huang, Y., Cui, B., Bai, L., Guo, Z., Xu, M., Ren, H.: Endo-4dgs: Distilling depth ranking for endoscopic monocular scene reconstruction with 4d gaussian splatting. arXiv preprint arXiv:2401.16416 (2024) 2
10. Jha, D., Smedsrud, P.H., Riegler, M.A., Halvorsen, P., de Lange, T., Johansen, D., Johansen, H.D.: Kvasir-seg: A segmented polyp dataset. In: MMM. pp. 451–462 (2020) 6, 7, 8
11. Li, Y., Hu, M., Yang, X.: Polyp-sam: Transfer sam for polyp segmentation. arXiv preprint arXiv:2305.00293 (2023) 1, 3, 7, 8
12. Loshchilov, I., Hutter, F.: Decoupled weight decay regularization. arXiv preprint arXiv:1711.05101 (2017) 6
13. Margolin, R., Zelnik-Manor, L., Tal, A.: How to evaluate foreground maps? In: Proceedings of the IEEE conference on computer vision and pattern recognition. pp. 248–255 (2014) 6
14. Patel, K., Bur, A.M., Wang, G.: Enhanced u-net: A feature enhancement network for polyp segmentation. In: 2021 18th Conference on Robots and Vision (CRV). pp. 181–188. IEEE (2021) 3

15. Poudel, S., Lee, S.W.: Deep multi-scale attentional features for medical image segmentation. Applied Soft Computing **109**, 107445 (2021) 3
16. Ronneberger, O., Fischer, P., Brox, T.: U-net: Convolutional networks for biomedical image segmentation. In: Navab, N., Hornegger, J., III, W.M.W., Frangi, A.F. (eds.) MICCAI 2015. pp. 234–241. LNCS, Springer (2015), https://doi.org/10.1007/978-3-319-24574-4_28 3, 7, 8
17. Shussman, N., Wexner, S.D.: Colorectal polyps and polyposis syndromes. Gastroenterology report **2**(1), 1–15 (2014) 1
18. Silva, J., Histace, A., Romain, O., Dray, X., Granado, B.: Toward embedded detection of polyps in WCE images for early diagnosis of colorectal cancer. CARS **9**, 283–293 (2014) 6, 8
19. Suvorov, R., Logacheva, E., Mashikhin, A., Remizova, A., Ashukha, A., Silvestrov, A., Kong, N., Goka, H., Park, K., Lempitsky, V.: Resolution-robust large mask inpainting with fourier convolutions. In: Proceedings of the IEEE/CVF winter conference on applications of computer vision. pp. 2149–2159 (2022) 3
20. Tajbakhsh, N., Gurudu, S.R., Liang, J.: Automated polyp detection in colonoscopy videos using shape and context information. IEEE TMI **35**(2), 630–644 (2015) 1, 6, 8
21. Tolstikhin, I.O., Houlsby, N., Kolesnikov, A., Beyer, L., Zhai, X., Unterthiner, T., Yung, J., Steiner, A., Keysers, D., Uszkoreit, J., et al.: Mlp-mixer: An all-mlp architecture for vision. Advances in neural information processing systems **34**, 24261–24272 (2021) 2, 4
22. Vázquez, D., Bernal, J., Sánchez, F.J., Fernández-Esparrach, G., López, A.M., Romero, A., Drozdzal, M., Courville, A., et al.: A benchmark for endoluminal scene segmentation of colonoscopy images. JHE **2017** (2017) 6, 8
23. Wang, J., Huang, Q., Tang, F., Meng, J., Su, J., Song, S.: Stepwise feature fusion: Local guides global. In: International Conference on Medical Image Computing and Computer-Assisted Intervention. pp. 110–120. Springer (2022) 1, 3, 7, 8
24. Wang, K.N., He, Y., Zhuang, S., Miao, J., He, X., Zhou, P., Yang, G., Zhou, G.Q., Li, S.: Ffcnet: Fourier transform-based frequency learning and complex convolutional network for colon disease classification. In: International Conference on Medical Image Computing and Computer-Assisted Intervention. pp. 78–87. Springer (2022) 3
25. Wei, J., Hu, Y., Zhang, R., Li, Z., Zhou, S.K., Cui, S.: Shallow attention network for polyp segmentation. In: Medical Image Computing and Computer Assisted Intervention–MICCAI 2021: 24th International Conference, Strasbourg, France, September 27–October 1, 2021, Proceedings, Part I 24. pp. 699–708. Springer (2021) 3, 7, 8
26. Wei, J., Wang, S., Huang, Q.: F^3net: fusion, feedback and focus for salient object detection. In: Proceedings of the AAAI conference on artificial intelligence. vol. 34, pp. 12321–12328 (2020) 5
27. Wu, H., Zhong, J., Wang, W., Wen, Z., Qin, J.: Precise yet efficient semantic calibration and refinement in convnets for real-time polyp segmentation from colonoscopy videos. In: Proceedings of the AAAI Conference on Artificial Intelligence. vol. 35, pp. 2916–2924 (2021) 3
28. Yang, L., Kang, B., Huang, Z., Xu, X., Feng, J., Zhao, H.: Depth anything: Unleashing the power of large-scale unlabeled data. arXiv preprint arXiv:2401.10891 (2024) 2
29. Yin, Z., Liang, K., Ma, Z., Guo, J.: Duplex contextual relation network for polyp segmentation. In: 2022 IEEE 19th International Symposium on Biomedical Imaging (ISBI). pp. 1–5. IEEE (2022) 3, 7, 8

30. Yu, H., Zheng, N., Zhou, M., Huang, J., Xiao, Z., Zhao, F.: Frequency and spatial dual guidance for image dehazing. In: European Conference on Computer Vision. pp. 181–198. Springer (2022) 3

31. Zhang, R., Li, G., Li, Z., Cui, S., Qian, D., Yu, Y.: Adaptive context selection for polyp segmentation. In: Medical Image Computing and Computer Assisted Intervention–MICCAI 2020: 23rd International Conference, Lima, Peru, October 4–8, 2020, Proceedings, Part VI 23. pp. 253–262. Springer (2020) 3, 7, 8

32. Zhao, X., Zhang, L., Lu, H.: Automatic polyp segmentation via multi-scale subtraction network. In: MICCAI. pp. 120–130 (2021) 1, 7, 8

33. Zhou, T., Zhang, Y., Zhou, Y., Wu, Y., Gong, C.: Can sam segment polyps? arXiv preprint arXiv:2304.07583 (2023) 1, 3

34. Zhou, T., Zhou, Y., He, K., Gong, C., Yang, J., Fu, H., Shen, D.: Cross-level feature aggregation network for polyp segmentation. Pattern Recognition **140**, 109555 (2023) 1, 3

35. Zhou, Z., Rahman Siddiquee, M.M., Tajbakhsh, N., Liang, J.: Unet++: A nested u-net architecture for medical image segmentation. In: Deep Learning in Medical Image Analysis and Multimodal Learning for Clinical Decision Support: 4th International Workshop, DLMIA 2018, and 8th International Workshop, ML-CDS 2018, Held in Conjunction with MICCAI 2018, Granada, Spain, September 20, 2018, Proceedings 4. pp. 3–11. Springer (2018) 7, 8